

# Colossal Ionic Conductivity in Interphase Strain-Engineered Nanocomposite Films

Chuanrui Huo,<sup>○</sup> Kun Xu,<sup>○</sup> Liyang Ma,<sup>○</sup> Tianyu Li, Hao Li, Xiaoyan Yang, Xiaojun Kuang, Shi Liu, Shiqing Deng,<sup>\*</sup> and Jun Chen<sup>\*</sup>



Cite This: *J. Am. Chem. Soc.* 2023, 145, 13623–13631



Read Online

ACCESS |



Metrics & More

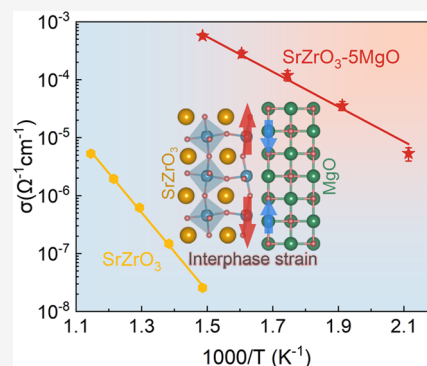


Article Recommendations



Supporting Information

**ABSTRACT:** Owing to their wide application in oxide-based electrochemical and energy devices, ion conductors have attracted considerable attention. However, the ionic conductivity of the developed systems is still too low to satisfy the low-temperature application. In this study, by developing the emergent interphase strain engineering method, we achieve a colossal ionic conductivity in SrZrO<sub>3</sub>-xMgO nanocomposite films, which is over one order of magnitude higher than that of the currently widely used yttria-stabilized zirconia below 673 K. Atomic-scale electron microscopy studies ascribe this superior ionic conductivity to the periodically well-aligned SrZrO<sub>3</sub> and MgO nanopillars that feature coherent interfaces. Wherein, a tensile strain as large as +1.7% is introduced into SrZrO<sub>3</sub>, expanding the *c*-lattice and distorting the oxygen octahedra to decrease the oxygen migration energy. Combining with theoretical assessments, we clarify the strain-dependent oxygen migration path and energy and unravel the mechanisms for strain-tuned ionic conductivity. This study provides a new scope for the property improvement of wide-range ion conductors by strain engineering.



## INTRODUCTION

Recent years have witnessed the prosperous development of many oxide-based electrochemical and energy devices, such as solid-oxide fuel cells (SOFCs),<sup>1–5</sup> memristors,<sup>6,7</sup> and oxygen separation membranes.<sup>8</sup> The transport performance of oxygen ions in the electrolytes is key to this technology because it essentially determines the conversion efficiency of the chemical-to-electrical energy.<sup>9</sup> However, current ion conductors are still limited by their high operating temperatures and inferior ionic conductivity at low temperatures, which greatly influences the near-room-temperature operation of these devices and hinders their further development.<sup>10</sup> For example, the temperature for adequate ionic conductivity of yttria-stabilized zirconia (YSZ) electrolytes, which are widely used in commercially available SOFCs, is as high as 1073 K.<sup>11</sup> Under this high working temperature, the practical application of SOFCs is limited by a series of severe problems including high cell costs and fast performance degradation.<sup>12</sup> Therefore, the development of high-performance oxygen ion conductors, especially at low operating temperatures, is highly desired for the development and performance optimization of practical devices, such as low-temperature ( $\leq 673$  K) solid-oxide fuel cells (LT-SOFCs); however, this remains a significant challenge.<sup>13,14</sup>

Because the conductivity performance of an ion conductor is highly sensitive to the strain states, much effort has been devoted to the strain-engineered enhancement of oxygen ion conductivity.<sup>15,16</sup> Typical strain engineering strategies include

dopant-induced chemical pressure,<sup>17</sup> interfacial strain in lateral multilayer systems,<sup>18–20</sup> vertical strain in vertically aligned nanocomposite (VAN) films,<sup>21,22</sup> and the interphase strain method.<sup>23</sup> Typically, chemical doping has been widely used in the property regulation of ion conductors, including rare earth ions (such as La<sup>3+</sup>, Nd<sup>3+</sup>, Sm<sup>3+</sup>, Gd<sup>3+</sup>, Dy<sup>3+</sup>, and Er<sup>3+</sup>) and alkali metal ions (such as Mg<sup>2+</sup>, Ca<sup>2+</sup>, and Sr<sup>2+</sup>).<sup>9,14</sup> For the interfacial strain engineering strategy in lateral multilayer systems, although some superior ionic conductivity has been achieved, further development of high-performance multilayer ion conductors in this context has been limited by the intrinsic drawbacks of the configuration, including the limited thickness and difficulty in application in devices that typically require out-of-plane conductivity.<sup>24</sup> Hence, films engineered by the vertical strain induced by the VAN structure or interphase strain have emerged as a promising configuration with outstanding performance that allows an out-of-plane conductivity channel and high strain tunability up to micrometer thickness.<sup>25,26</sup> In particular, the interphase strain engineering method can introduce large modulations of lattice strain by combining two phases with different lattice parameters and an

Received: February 4, 2023

Published: June 16, 2023



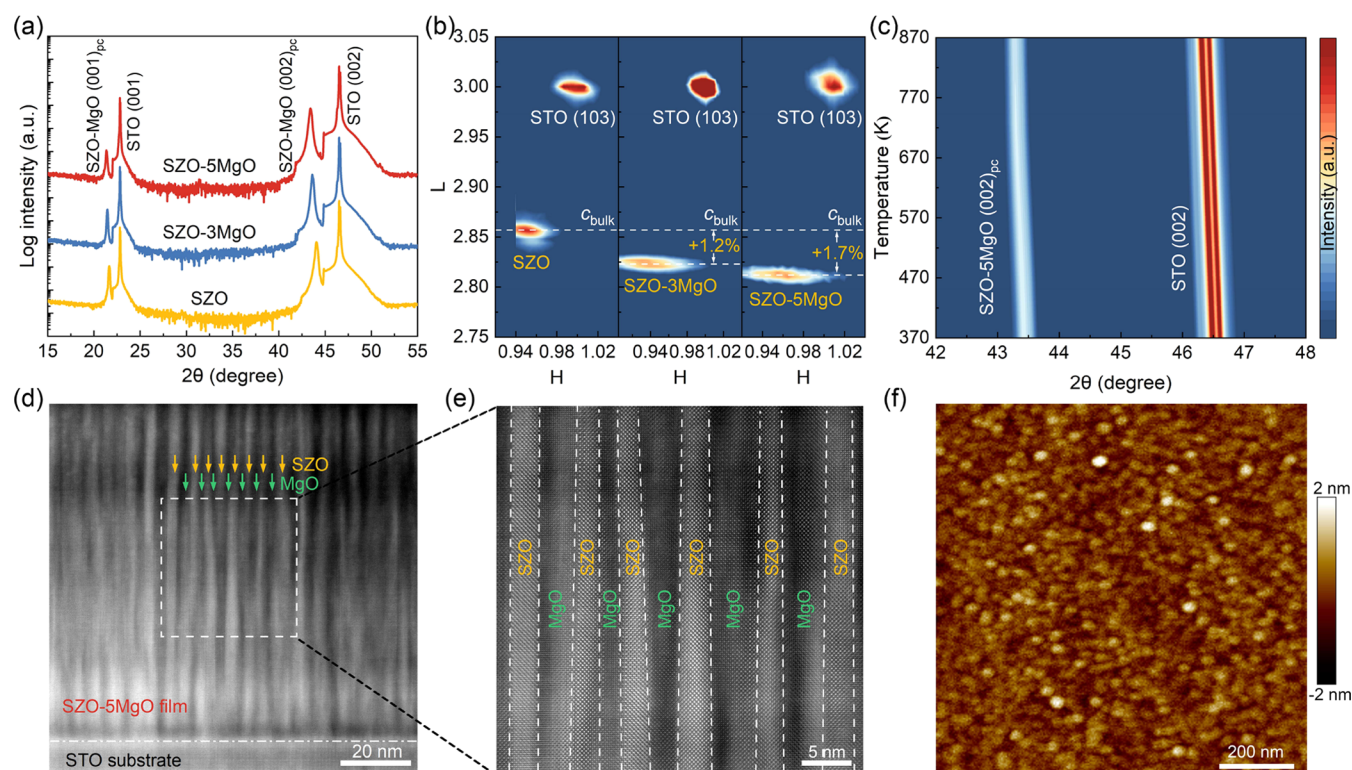


**Figure 1.** Structural characterization of SZO- $x$ MgO ( $x = 0, 3,$  and  $5$ ) films. (a) Out-of-plane XRD spectra for SZO- $x$ MgO ( $x = 0, 3,$  and  $5$ ) films on the (001)-orientated STO substrate. (b) Synchrotron-based reciprocal space mapping (RSM) studies around the STO substrate (103) diffraction for the SZO- $x$ MgO ( $x = 0, 3,$  and  $5$ ) films, where H and L represent the ( $h00$ ) and ( $00l$ ) Miller indices, respectively. (c) Temperature dependence of the out-of-plane XRD spectra for the SZO-5MgO film. (d) Low-mag cross-sectional HAADF-STEM image of the SZO-5MgO film. (e) Atomic-scale HAADF-STEM image, enlarged from the dashed rectangle framed region in panel (d), showing the periodic alignment of the SZO and MgO phases. (f) Surface topography of the SZO-5MgO film.

atomically coherent interface between them.<sup>23</sup> Such interphase strain is also uniform and unrelaxed along the film thickness direction. The application of the interphase strain engineering method in classic ferroelectrics has harvested giant ferroelectricity, highlighting its high effectiveness in modulating the material lattice.<sup>27,28</sup> This, therefore, suggests new possibilities and opportunities for improving the performance of lattice-strain-sensitive oxygen ion conductivity.

Oxides with a perovskite structure (general formula:  $ABO_3$ ) can accommodate a wide range of cations and are among the most versatile classes of SOFCs.<sup>29–31</sup> Among them, perovskite strontium zirconate,  $SrZrO_3$  (SZO), with an orthorhombic  $GdFeO_3$ -type structure (space group  $Pbnm$ , No. 62), is a representative ion conductor for protons and oxygen ions.<sup>32–34</sup> Although pure SZO has a working temperature higher than 1273 K, its ionic conductivity and working temperature have been demonstrated to scale with strain,<sup>22</sup> suggesting its high tunability by strain engineering. For example, with an increase in the tensile strain in SZO, the ionic conductivity can increase by one order of magnitude.<sup>22</sup> Even though the strain effect has been well-recognized to be critical in SZO and other ion conductors, the manner in which strain functions remains elusive. Thus, it is of great scientific importance to unravel the underlying mechanism of strain engineering to elucidate the nature and origin of the property enhancement in strained SZO, which could lay the foundation for further strain-based ionic conductivity performance improvement.

In this study, through the introduction of the interphase strain using a binary oxide MgO (space group  $Fm-3m$ , No. 225), we not only achieved a colossal ionic conductivity in

SZO- $x$ MgO nanocomposite films but also unambiguously unraveled the underlying strain-tuning mechanisms. The MgO phase was chosen because it has a similar alternating arrangement of the atomic plane to SZO and a larger  $c$ -axial lattice parameter, which can effectively introduce the desired tensile strain into the SZO phase. More importantly, it is immiscible with the SZO phase. Thus, in contrast to previous studies using MgO as dopants for performance improvement, such as  $La_{0.9}Sr_{0.1}Ga_{0.8}Mg_{0.2}O_{3-\delta}$  (LSGM)<sup>17,24</sup> and  $Na_{0.5}Bi_{0.49}Ti_xMg_{1-x}O_{3-\delta}$  (NBT),<sup>30</sup> the MgO in this study acts as an individual secondary phase, as evidenced by our experimental results. The ionic conductivity realized ( $5.67 \times 10^{-4} \text{ S cm}^{-1}$  at 673 K) is increased by as much as four orders of magnitude compared to that of bulk SZO and over one order of magnitude higher than that of YSZ below 673 K. Advanced scanning transmission electron microscopy (STEM) investigations revealed the microstructures of SZO-MgO nanocomposite films that feature two periodically aligned phases of SZO ( $\sim 3$  nm) and MgO ( $\sim 5$  nm) nanopillars with coherent interfaces, where, based on atomic-scale quantifications, the SZO nanopillar is under a tensile strain as high as 1.7%. Combining these results with theoretical calculations, we clarify the strain-dependent oxygen migration path and unravel the origin of the enhanced ionic conductivity caused by strain. The findings of this work provide new insights into material design and new opportunities for the property improvement of the entire ion conductor family and advance our understanding of the nature of ionic conductivity.

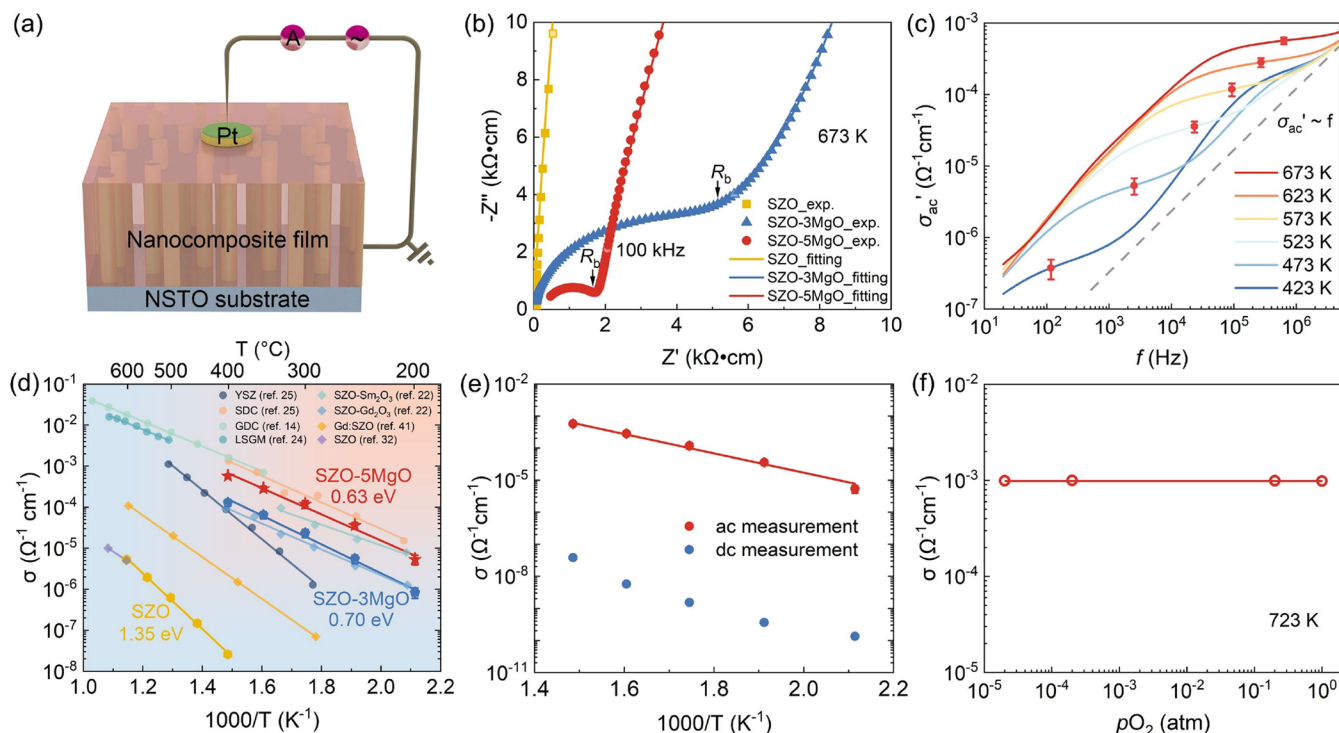


**Figure 2.** Ionic conductivity of the SZO- $x$ MgO ( $x = 0, 3,$  and  $5$ ) films. (a) Schematic illustrations of the nanopillar structure and out-of-plane transport measurement configuration. (b) Impedance spectra (Nyquist plots) of the SZO- $x$ MgO ( $x = 0, 3,$  and  $5$ ) films at 673 K. (c) Double log plot of the  $f$ -dependent real part of the alternating current (ac) conductivity  $\sigma_{ac}'$  for the SZO-5MgO film in the temperature range of 423–673 K. Gray dashed line represents a near-constant (dielectric) loss. Red solid circles indicate the value of long-range ionic conductance. Error bars are the uncertainty of platform positions. (d) Comparison of the ionic conductance for the SZO- $x$ MgO ( $x = 0, 3,$  and  $5$ ) films with those of previous studies. (e) Arrhenius plot of ionic conductivity for the SZO-5MgO film obtained by ac measurement and the direct current (dc) measurements. (f) Oxygen partial pressure ( $p_{O_2}$ ) dependence of the ionic conductivity for the SZO-5MgO film.

## RESULTS AND DISCUSSION

SZO- $x$ MgO ( $x = 0, 3,$  and  $5$ , where  $x$  represents the molar ratio of the MgO and SZO phases) films were grown on (001)-oriented SrTiO<sub>3</sub> (STO) substrates by pulsed laser deposition (PLD) with carefully designed polycrystalline composite targets (see Methods for details). The real compositions of the thin films were determined by inductively coupled plasma-optical emission spectroscopy (ICP-OES) measurements, as summarized in Table S1. The X-ray diffraction (XRD) results (Figure 1a) confirmed the (001)<sub>pc</sub>-oriented (pc refers to pseudocubic indices) epitaxial growth and high crystallinity of all the films. Combined with the reciprocal space mapping (RSM) in Figure 1b, the out-of-plane and in-plane lattice parameters of the pure SZO thin film ( $x = 0$ ) were both determined to approximate the bulk value of 4.10 Å, indicating the strain-free state of the obtained pure SZO thin film.<sup>35</sup> Upon introducing the MgO phase, the (001) peaks markedly shifted to lower angles (blue and red spectra in Figure 1a), indicating the evident expansion of the  $c$ -axial lattice spacing of the SZO-3MgO and SZO-5MgO films. Notably, only a single set of (001) diffraction peaks (Figure 1a) was detected, implying well-matched interfaces in the out-of-plane direction of the SZO and MgO phases. This was also confirmed by the combination of our atomic-scale microscopy characterizations (Figure 1e), RSM study around the (111) diffraction (Figure S1a), and energy-dispersive X-ray spectroscopy (EDXS) elemental mapping (Figure S2). With the increase in the MgO content, the out-of-plane lattices of the films gradually expanded from +1.2% in the SZO-3MgO film to +1.7% in the

SZO-5MgO film (Figure 1a), as evidenced by the RSM results (middle and right panels of Figure 1b). The evolutions of the lattice and strain states are summarized in Figure S1b and Table S2. In addition, the temperature-dependent out-of-plane XRD results in Figure 1c confirm the high thermal stability and robustness of the films. As shown in Figure 1c, the strained SZO-5MgO film exhibited no detectable phase transition, even up to 870 K.

Cross-sectional aberration-corrected STEM investigations were performed to examine the microstructure of the SZO-5MgO film, in particular, the spatial assembly of the SZO and MgO phases. As shown in the low-mag high-angle annular dark-field (HAADF)-STEM image in Figure 1d, the SZO (indicated by yellow arrows) and MgO (indicated by green arrows) phases feature as nanopillars and manifest an alternative distribution with long-range periodicity in the lateral direction (EDXS mapping results are shown in Figure S2). More importantly, the interfaces between the SZO and MgO phases are coherent and atomically sharp, as evidenced by the atomically resolved HAADF-STEM image in Figure 1e, which is an enlargement of the white dashed rectangular region in Figure 1d. The lateral dimensions of the SZO and MgO nanopillars are uniform and within the range of 2–5 nm. Figure 1f displays the atomic force microscopy (AFM) characterization of the film surface, which shows the dotted surface topography and is consistent with the phase-separating nanopillar structure. Notably, the out-of-plane  $c$ -parameters of the strain-free SZO and MgO are  $c_{SZO} = 4.10$  Å and  $c_{MgO} = 4.20$  Å, respectively.<sup>35,36</sup> Thus, combining the SZO and MgO phases together with a coherent interface, as evidenced by the

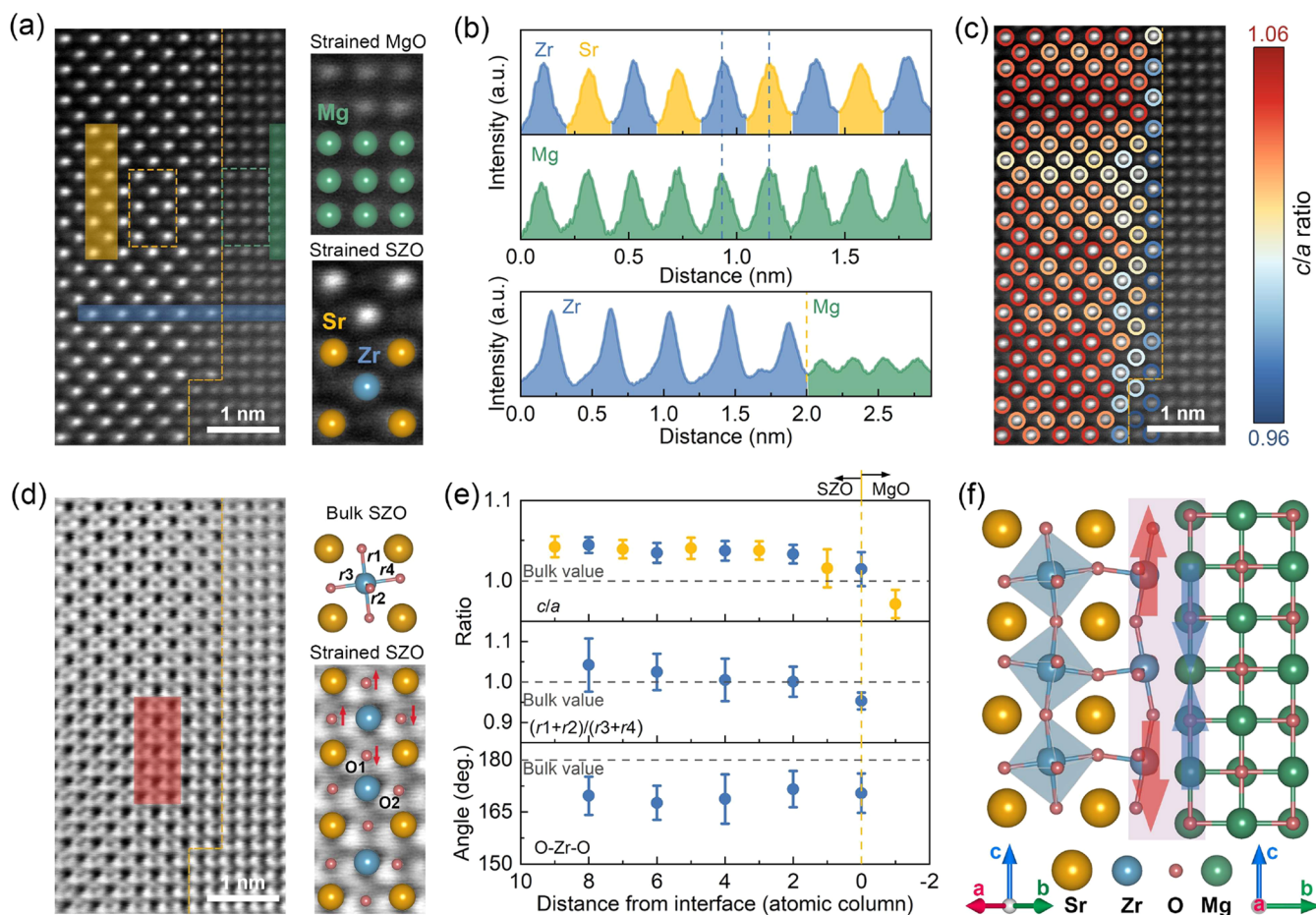


**Figure 3.** Atomic-scale characterization of the SZO–5MgO film. (a) HAADF-STEM image of the SZO–MgO interface viewed along the [100] axis of MgO. Enlarged images from the yellow- and green-dashed rectangle-frame regions on the right side show the unit cells of the strained SZO and MgO, respectively. (b) Intensity profiles of atomic columns extracted from the yellow (parallel to the interface, top panel), green (parallel to the interface, middle panel), and blue (across the interface, bottom panel) shaded areas in panel (a). (c) Color-mapped  $c/a$  ratio of the SZO phase superimposed with the same region in panel (a). (d) ABF-STEM image of the same region is shown in panel (a). The top right panel is the  $[100]_{pc}$  axial crystal model for the bulk SZO, indicating the four Zr–O bonds in the oxygen octahedron. The bottom right panel shows the magnified images from the pink-shaded region with the atomic models overlaid. Red arrows indicate the oxygen displacement. (e) Average line profile of the  $c/a$  ratio, O–Zr–O angle, and  $(r1+r2)/(r3+r4)$  value of the whole region in panel (a) across the SZO–MgO interface. The error bars are the standard deviation. (f) Schematic structural model for the coherent SZO–MgO interface, which is constructed based on atomic-scale observations.

HAADF-STEM image, introduces tensile and compressive strains into the SZO and MgO phases, respectively. Therefore, the changes in the average out-of-plane lattice in the SZO– $x$ MgO films, as indicated by the XRD results (Figure 1a,b), should be dominated by the lattice matching of the two phases (Figure S3) that eventually reach a balanced state with the same  $c$ -parameter (larger than that of bulk SZO and smaller than that of bulk MgO) rather than display the clamping effect of the substrate. Moreover, the fast Fourier transform (FFT) of the atomically resolved low-magnification HAADF-STEM image (Figure S4) further confirms the matching relationship between the SZO and MgO phases as well as the STO substrate.

The ionic conductivity properties of these interphase strain-tuned SZO– $x$ MgO ( $x = 0, 3, \text{ and } 5$ ) films were characterized by the widely used frequency ( $f$ )-dependent ac impedance spectrum.<sup>37–42</sup> Considering the vertical nanopillar structure, we adopted a top-down out-of-plane transport configuration for the measurements,<sup>20,25</sup> as shown in Figure 2a. The ion-blocking Pt dots and Nb-doped STO (NSTO) substrate serve as the top and grounded bottom electrodes, respectively.

Figure 2b demonstrates the Nyquist plots for the SZO– $x$ MgO ( $x = 0, 3, \text{ and } 5$ ) films at 673 K, wherein with the increase in the tensile strain, a significant reduction in the bulk resistance ( $R_b$ , extract from the high-frequency arc) can be observed. The measured frequency-dependent resistance data can then be converted into frequency-dependent conductivity data using the formula  $\sigma = L/RS$  ( $R$  is the resistance of the thin film,  $S$  is the top Pt electrode area, and  $L$  is the thin film thickness). To precisely determine the ionic conductivity of the SZO–5MgO film, we plotted the  $f$ -dependent real part conductance ( $\sigma_{ac}'$ ) in a double logarithmic diagram (Figure 2c) and compared it with widely used equivalent circuit fitting methods (Figure S5). Generally,  $\sigma_{ac}'$  decreases with a decrease in  $f$  at both high-frequency ( $\sigma_{ac}' \sim f$ , a nearly constant dielectric loss due to short-range ion migration) and low-frequency (due to the electrode polarization effect) regions, whereas it is independent of  $f$  at intermediate frequencies, showing a platform that is a characteristic electrical response of ion conductors with ion-blocking electrodes (Figure 2c).<sup>19,25,43</sup> This  $f$ -independent platform (as indicated by circles) corresponds to the direct current (dc) conductivity of ions due to long-range ion

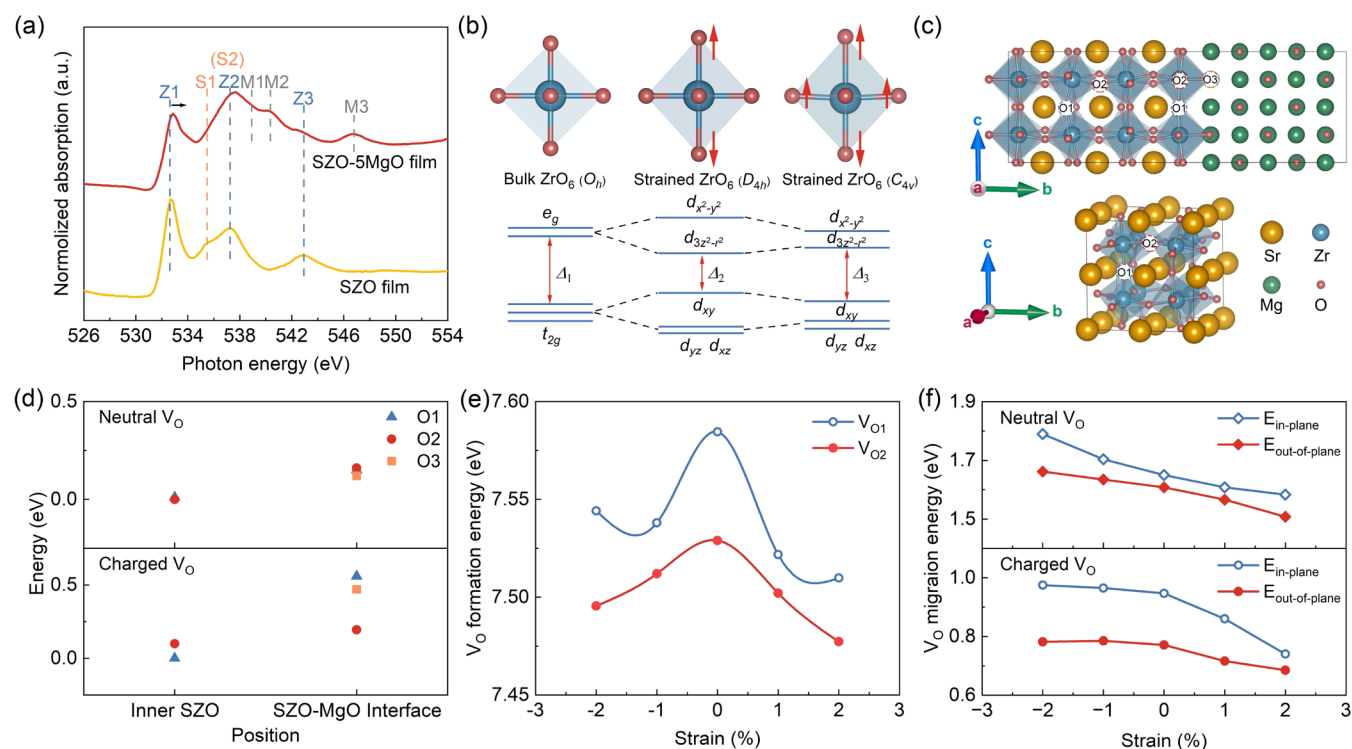


**Figure 4.** Electronic structure and DFT calculations on the origin of the strain-enhanced ionic conductivity of the SZO–5MgO film. (a) O K-edge XAS of pure SZO and the SZO–5MgO film. Absorption peaks of the Zr 4d, Sr 4d, Zr 5s, and Mg s, p orbitals are noted as Z1, Z2, S1, S2, Z3, M1, M2, and M3, respectively. (b) Schematic of the evolution of the  $\text{ZrO}_6$  octahedra and corresponding orbital configurations under strain. (c) Calculation models of the SZO–MgO nanocomposite (top panel) and single strained SZO phase (bottom panel). (d) Comparison of the system energy with different oxygen vacancies at the SZO–MgO interface and inner SZO, based on assumptions of the neutral (top panel) and charged oxygen vacancy (bottom panel). Note that the lowest system energy was set to zero for comparison. (e) Out-of-plane strain-dependent oxygen vacancy formation energy for neutral oxygen sites in SZO. (f) Out-of-plane strain-dependent oxygen vacancy migration energy along the different directions in SZO based on neutral (top panel) and charged oxygen vacancy (bottom panel).

transport. Because the dc conductivity of ions is thermally activated, it is enhanced with increasing temperature, as shown in Figure 2c. In addition, a spike-like tail at low frequency (Warburg impedance) (Figure S5a) confirms the ionic conductivity of the SZO–5MgO film.<sup>44</sup>

We next determined the ionic conductance of the SZO and SZO–3MgO films and compared our achieved performance with previously reported results for typical ion conductors (Figure 2d). For the pure SZO/STO thin film, owing to its intrinsically poor ionic conductivity,<sup>32</sup> a relatively high temperature is required to obtain an observable conductance. As expected, the measured alternating current (ac) ionic conductance of the pure SZO/STO film was at a low level ( $2.56 \times 10^{-8} \text{ S cm}^{-1}$  at 673 K), as indicated by the yellow lines in Figure 2d, which is consistent with the value of the SZO ceramic.<sup>32</sup> This not only manifests the high quality of the thin film but also suggests that the SZO–STO interfacial strain is not the dominant factor for the observed ionic conductivity improvement. Upon introducing a tensile strain (+1.2%) into SZO by adding the MgO phase in the SZO–3MgO film, the ionic conductivity ( $1.29 \times 10^{-4} \text{ S cm}^{-1}$  at 673 K) displayed substantial enhancement (blue lines), which was over three orders of magnitude higher than those of the strain-free pure SZO thin film and Gd-doped SZO bulk.<sup>45</sup> Further increasing the tensile strain (+1.7%) enhanced the ionic conductivity ( $5.67 \times 10^{-4} \text{ S cm}^{-1}$  at 673 K) by half order of magnitude in the SZO–5MgO film (red lines) compared to the SZO–3MgO film, highlighting the critical role of the SZO–MgO

interphase strain. Notably, such superior ionic conductivity is an order of magnitude higher than that of classic YSZ films below 673 K.<sup>14</sup> The ionic conductivities remain nearly constant across the range of film thicknesses we tested (Figure S6), which further confirms that the interphase strain is uniform and unrelaxed along the film thickness direction. Moreover, the ac measurements showed good stability and repeatability with different electrode positions (Figure S7), which suggests the homogeneity of the thin film and excludes possible short-circuiting and extrinsic contributions. To rule out the possible contribution of electronic conduction, dc measurements (constant voltage method)<sup>19,25</sup> were conducted using the same electrode configuration and equipment as those used for the ac measurement. The large differences between the ac and dc methods (Figure 2e) indicate that the conductivity of the film is dominated by the ionic conductivity and that the electrical conduction (four magnitudes lower) is negligible. In addition, as shown in Figures 2f and S8, measurements of the ac impedance in different atmospheres manifested negligible differences, which further confirms the ionic conductivity of our sample and suggests its robustness.

To reveal the origin of the significantly enhanced ionic conductivity from the microscopic viewpoint, we performed atomic-scale quantitative analyses based on spherical aberration-corrected STEM. The atomically resolved HAADF-STEM images (Figures 3a and S9) show a typical SZO–MgO interface in the film, which is atomically sharp and well-matched for the two phases in each atomic layer. Combining

the crystal structure data (SZO,  $Pbnm$ ; MgO,  $Fm-3m$ ), the simulated STEM images (Figure S10), and the atomic column brightness that is approximately proportional to  $Z^{1.7}$  ( $Z$  is the atomic number),<sup>46</sup> the left side of the image can be determined as the SZO phase at the  $[110]$  zone axis, while the right side is the MgO phase along the  $[100]$  zone axis. Moreover, a detailed analysis of the atomic intensities (upper panel of Figure 3b) in the yellow rectangular shaded region in Figure 3a further differentiates the Sr–O and Zr–O planes in SZO. On this basis, the matching fashion of the two phases can be revealed (Figures 3f and S11), where the Sr–O and Zr–O planes match the O–Mg and Mg–O planes, respectively. In addition, the intensity profile across the interface indicates a near-bulk in-plane lattice parameter for both SZO and MgO, which is consistent with the RSM results. Based on the fitted atomic positions (see details in the Methods), we calculated the  $c/a$  ratios and mapped them in Figure 3c to inspect the changes in the SZO lattice. It can be seen that almost all the SZO unit cells possess  $c/a$  ratios larger than unity, suggesting the strong tetragonal distortion of the SZO lattice introduced by MgO and well agreeing with the XRD results. Notably, the SZO phase is uniformly distorted for regions near or away from the SZO–MgO and SZO–STO interfaces; that is, the entire SZO nanopillar is fully strained (see also the statistical results in Figure 3e). This should have its origin in the nanoscale lateral dimensions of both the SZO and MgO pillars. Such an increased  $c$ -directional lattice spacing of SZO can therefore provide an enlarged migration channel for ions, which benefits from the increase in ionic conductivity.<sup>9</sup>

Atomic-scale annular bright-field (ABF) images with visible oxygen atoms were also acquired (Figure 3d) and quantitatively analyzed to elucidate the oxygen environment. As shown in the bottom right panel of Figure 3d, the oxygen octahedra of the strained SZO, enlarged from the pink-shaded area, show distinct distortion compared with the crystal structure of bulk SZO (top right panel of Figure 3d). Specifically, both O1 (located in the Sr–O planes) and O2 (located in the Zr–O planes) atoms manifest distinct  $c$ -directional displacements, as indicated by the red arrows in the bottom right panel of Figure 3d, resulting in changes in the Zr–O bond lengths and O–Zr–O bond angles. As shown in the middle panel of Figure 3e, the ratio of the out-of-plane and in-plane Zr–O lengths  $((r1 + r2)/(r3 + r4))$  is significantly increased, suggesting the elongation of the  $ZrO_6$  octahedra with a weakened Zr–O2 hybridization strength. Meanwhile, owing to the out-of-plane displacement of O2, the O–Zr–O angle (bottom panel of Figure 3e) also significantly deviates from the bulk angle ( $180^\circ$ ). Consistent with the quantitative results of the  $c/a$  ratios in Figure 3c and the top panel of Figure 3e, the distortions of the oxygen octahedra are almost independent of the distance from the SZO–MgO interface and uniform across the entire SZO nanopillars. Based on these observations and quantification, a structural model for the SZO–MgO interface was constructed (Figure 3f), where the bonding configurations are clearly demonstrated. With a coherent interface between the SZO and MgO phases, the larger (smaller) lattice-phase MgO (SZO) imposes a tensile (compressive) strain on the smaller (larger) lattice-phase SZO (MgO).

To establish the strain-tuned microstructure-ionic conductivity relationship, we examined the local electronic structures of SZO using X-ray absorption spectroscopy (XAS)<sup>47–49</sup> and conducted first-principles density functional

theory (DFT) calculations. Figure 4a shows the O  $K$ -edge XAS spectra of the SZO–5MgO film. According to crystal field theory, an ideal  $ZrO_6$  octahedron configuration contains doubly degenerate high-energy  $e_g$  orbitals and triply degenerate low-energy  $t_{2g}$  orbitals (Figure 4b). These degenerated orbitals split into suborbital when the octahedron is distorted. Consequently, the elongation of  $ZrO_6$  along the out-of-plane direction in the strained SZO introduces orbital splitting, as illustrated in Figure 4b. Although this out-of-plane elongation can weaken the hybridization between the Zr and O atoms, the O atoms are further shifted to minimize the total energy. Owing to the displacement of O atoms along the out-of-plane direction, the hybridization between Zr and O1 is strengthened, while that between Zr and O2 becomes weaker, which increases the overlap degree of Zr 4d and O1 2p orbitals (Figure S12) and decreases the relative intensity of the Zr 4d  $t_{2g}$  and  $e_g$  orbitals (Figure 4a). Moreover, such distortion eventually decreases the splitting energy ( $\Delta_3$ ), which is consistent with the high-energy shift of the Zr 4d  $t_{2g}$  peak (Figure 4a). Therefore, the strain-enhanced ionic conductivity in the SZO–5MgO film originates from the weakened Zr–O2 hybridization and the increased space that facilitates vacancy production and ion migration. This speculation was further confirmed by DFT calculations.

The favorable formation positions of oxygen vacancies were determined first. We constructed the SZO–MgO interface model (top panel in Figure 4c) based on atomic-scale experimental observations (Figure 3) for calculations. We then calculated and compared the system energies for structures with oxygen vacancies located at the inner SZO and the SZO–MgO interfaces, as shown in Figure 4d. Both neutral ( $V_O^0$ ) and charged ( $V_O^{2+}$ ) states of O vacancies were considered in our calculations. Our results indicate that regardless of whether the calculation was based on the  $V_O^0$  or  $V_O^{2+}$ , the system with oxygen vacancies in the inner SZO always has the lowest energy. This suggests that oxygen vacancies are more likely to be produced in the uniformly stretched SZO phase rather than at the interface. Furthermore, we conducted further calculations to establish the relationship between oxygen vacancy positions, strain states, and ionic conductivity. Owing to the distorted oxygen octahedra in SZO, two distinct oxygen sites (O1 and O2) were considered (bottom panel in Figure 4c). As shown in Figure 4e, out-of-plane expansion can decrease the oxygen vacancy formation energy compared to that in strain-free SZO. Besides, carefully controlled growth conditions and annealing processes are also required to facilitate the formation of oxygen vacancies. As expected, the energy of the oxygen vacancy at the O2 site was lower than that at the O1 site, which supports the microscopy analysis data of the weakened hybridization of the Zr–O2 bond. Furthermore, to elucidate the preferential ion migration paths, we examined the strain-dependent ion migration energy both along the out-of-plane and in-plane directions (Figure 4f). A  $V_O^{2+}$  migration energy (0.68 eV) under 2% tensile strain was obtained, which is well consistent with the experimental results (0.63 eV). It is noteworthy that the migration energies of oxygen vacancies display a consistent decreasing trend with increasing tensile strain, independent of the oxygen vacancy's charge state (neutral or charged) as shown in Figure 4f, and irrespective of the density functional employed in the calculations, as demonstrated in Figure S13. This further confirms the crucial role of tensile strain in enhancing ionic conductivity. Notably, both the in-plane and out-of-plane  $V_O$

migration energies can be reduced by the *c*-axial tensile strain, corresponding to improvements in both the in-plane and out-of-plane ionic conductivities. Nevertheless, long-range in-plane conductivity is unattainable in practice because the in-plane migration of ions would be hindered by the vertical SZO–MgO interface. This agrees with previous theoretical studies that tensile strain can enhance the diffusivity of ions regardless of the pathways.<sup>24</sup>

Compared to the strain-free SZO film, the strain-mediated considerable reduction in oxygen migration energy (0.7 and 1.35 eV for SZO–3MgO and strain-free SZO film, respectively) is the dominant factor responsible for the significant enhancement in ionic conductivity in the interphase strain-engineered SZO–3MgO film. While comparing SZO–5MgO (0.63 eV) and SZO–3MgO (0.7 eV), it is worth noting that a further increase in the lattice strain would not reduce the activation energy to the same extent. However, the ionic conductivity would still show a further evident increase. This suggests that the further enhancement in ionic conductivity, when the oxygen migration energy is sufficiently low, should be mainly contributed by an increase in the concentration of oxygen vacancies (Figure 4e), which is consistent with previous studies.<sup>22,24,25</sup> We also note that the reduction rate of activation energy with increasing tensile strain is smaller in calculations than in experiments, which could be attributed to various factors. One is that the oxygen vacancy types present in practical SZO–*x*MgO (*x* = 0, 3, 5) films can be a mixture of different ratios of  $V_{\text{O}}^0$  and  $V_{\text{O}}^{2+}$ , which have different sensitivities to strain variations, as evidenced in Figure 4f. Additionally, despite our efforts to consider as many as possible factors in our calculations, such as the charge states of oxygen vacancies, certain complex conditions for SZO in practice, such as local fluctuations in strain states or electronic structures, cannot be fully captured by DFT calculations. Nevertheless, our calculations underscore the crucial role of tensile strain in enhancing ionic conductivity and clarifying the lowest-energy migration path of oxygen ions. This finding provides further insight into the origin of strain-enhanced ionic conductivity.<sup>22</sup>

## CONCLUSIONS

Using the interphase strain engineering method, we designed and fabricated a series of well-assembled SZO–*x*MgO (*x* = 0, 3, and 5) nanocomposite films and achieved a significant enhancement in the ionic conductivity. In particular, a superior ionic conductivity that was four orders of magnitude higher than that of bulk SZO and one order of magnitude higher than that of the widely used YSZ below 673 K was realized in the SZO–5MgO films. Advanced electron microscopy investigations revealed the atomic-scale structures and strain states of the films, where through the coherent interfaces between the SZO and MgO phases, a tensile strain as high as +1.7% was introduced into the SZO to significantly distort the lattice, particularly the oxygen octahedra. Combining these results with the DFT calculation results, we established the relationship between the tensile strain-tuned microstructure and oxygen migration behaviors, based on which the strain-tuning mechanism was elucidated. This study provides new scope for the design and property improvement, not only for the large ionic family but also for wide-ranging strain-sensitive functional materials, which would steer the exploration toward the design and development of new high-performance materials.

## ASSOCIATED CONTENT

### Supporting Information

The Supporting Information is available free of charge at <https://pubs.acs.org/doi/10.1021/jacs.3c01298>.

Additional experimental details for thin film growth, structural characterizations, electrical measurements, and DFT calculation (PDF)

## AUTHOR INFORMATION

### Corresponding Authors

**Shiqing Deng** – Beijing Advanced Innovation Center for Materials Genome Engineering, Department of Physical Chemistry, University of Science and Technology Beijing, Beijing 100083, China; School of Mathematics and Physics, University of Science and Technology Beijing, Beijing 100083, China; Email: [sqdeng@ustb.edu.cn](mailto:sqdeng@ustb.edu.cn)

**Jun Chen** – Beijing Advanced Innovation Center for Materials Genome Engineering, Department of Physical Chemistry, University of Science and Technology Beijing, Beijing 100083, China; [orcid.org/0000-0002-7330-8976](https://orcid.org/0000-0002-7330-8976); Email: [junchen@ustb.edu.cn](mailto:junchen@ustb.edu.cn)

### Authors

**Chuanrui Huo** – Beijing Advanced Innovation Center for Materials Genome Engineering, Department of Physical Chemistry, University of Science and Technology Beijing, Beijing 100083, China

**Kun Xu** – School of Materials Science and Engineering, Tsinghua University, Beijing 100084, China; Department of Mechanical Engineering, Stanford University, Stanford, California 94305, United States

**Liyang Ma** – Key Laboratory for Quantum Materials of Zhejiang Province, Department of Physics, School of Science, Westlake University, Hangzhou, Zhejiang 310024, China

**Tianyu Li** – Beijing Advanced Innovation Center for Materials Genome Engineering, Department of Physical Chemistry, University of Science and Technology Beijing, Beijing 100083, China; [orcid.org/0000-0001-8857-433X](https://orcid.org/0000-0001-8857-433X)

**Hao Li** – Beijing Advanced Innovation Center for Materials Genome Engineering, Department of Physical Chemistry, University of Science and Technology Beijing, Beijing 100083, China; [orcid.org/0000-0002-8952-5932](https://orcid.org/0000-0002-8952-5932)

**Xiaoyan Yang** – College of Chemistry and Bioengineering, Guilin University of Technology, Guangxi Key Laboratory of Optical and Electronic Materials and Devices, Guilin 541004, China; [orcid.org/0000-0003-2493-7079](https://orcid.org/0000-0003-2493-7079)

**Xiaojun Kuang** – College of Chemistry and Bioengineering, Guilin University of Technology, Guangxi Key Laboratory of Optical and Electronic Materials and Devices, Guilin 541004, China; [orcid.org/0000-0003-2975-9355](https://orcid.org/0000-0003-2975-9355)

**Shi Liu** – Key Laboratory for Quantum Materials of Zhejiang Province, Department of Physics, School of Science, Westlake University, Hangzhou, Zhejiang 310024, China; Institute of Natural Sciences, Westlake Institute for Advanced Study, Hangzhou, Zhejiang 310024, China; [orcid.org/0000-0002-8488-4848](https://orcid.org/0000-0002-8488-4848)

Complete contact information is available at: <https://pubs.acs.org/doi/10.1021/jacs.3c01298>

### Author Contributions

○C.H., K.X., and L.M. contributed equally to this work.

## Notes

The authors declare no competing financial interest.

## ACKNOWLEDGMENTS

This work was supported by the National Natural Science Foundation of China (Grant Nos. 21825102, 22001014, and 22090042), the Fundamental Research Funds for the Central Universities, China (Grant Nos. 06500162 and 06500145), the National Postdoctoral Program for Innovative Talents (Nos. BX20200043 and BX20200044), the China Postdoctoral Science Foundation (Grant No. 2021M690366), and State Key Laboratory of New Ceramic and Fine Processing Tsinghua University (Grant No. KF202110). This research used the resources of the Beijing National Center for Electron Microscopy at Tsinghua University and the Beijing Synchrotron Radiation Facility (1W1A and 4B9B beamlines) of the Chinese Academy of Science. C. Huo, K. Xu, and L. Ma contributed equally to this work. J.C. acknowledges the financial support of the University of Padova through the Visiting Scientist program 2019.

## REFERENCES

- (1) Steele, B. C. H.; Heinzel, A. Materials for fuel-cell technologies. *Nature* **2001**, *414*, 345–352.
- (2) Ormerod, R. M. Solid oxide fuel cells. *Chem. Soc. Rev.* **2003**, *32*, 17–28.
- (3) Mahato, N.; Banerjee, A.; Gupta, A.; Omar, S.; Balani, K. Progress in material selection for solid oxide fuel cell technology: A review. *Prog. Mater. Sci.* **2015**, *72*, 141–337.
- (4) Zheng, Y.; Wang, J.; Yu, B.; Zhang, W.; Chen, J.; Qiao, J.; Zhang, J. A review of high temperature co-electrolysis of H<sub>2</sub>O and CO<sub>2</sub> to produce sustainable fuels using solid oxide electrolysis cells (SOECs): advanced materials and technology. *Chem. Soc. Rev.* **2017**, *46*, 1427–1463.
- (5) Zhao, C.; Li, Y.; Zhang, W.; Zheng, Y.; Lou, X.; Yu, B.; Chen, J.; Chen, Y.; Liu, M.; Wang, J. Heterointerface engineering for enhancing the electrochemical performance of solid oxide cells. *Energy Environ. Sci.* **2020**, *13*, 53–85.
- (6) Strukov, D. B.; Snider, G. S.; Stewart, D. R.; Williams, R. S. The missing memristor found. *Nature* **2008**, *453*, 80–83.
- (7) Schweiger, S.; Pfenninger, R.; Bowman, W. J.; Aschauer, U.; Rupp, J. L. Designing Strained Interface Heterostructures for Memristive Devices. *Adv. Mater.* **2017**, *29*, No. 1605049.
- (8) Dyer, P. N.; Richards, R. E.; Russek, S. L.; Taylor, D. M. Ion transport membrane technology for oxygen separation and syngas production. *Solid State Ionics* **2000**, *134*, 21–33.
- (9) Skinner, S. J.; Kilner, J. A. Oxygen ion conductors. *Mater. Today* **2003**, *6*, 30–37.
- (10) Brett, D. J. L.; Atkinson, A.; Brandon, N. P.; Skinner, S. J. Intermediate temperature solid oxide fuel cells. *Chem. Soc. Rev.* **2008**, *37*, 1568–1578.
- (11) Malavasi, L.; Fisher, C. A.; Islam, M. S. Oxide-ion and proton conducting electrolyte materials for clean energy applications: structural and mechanistic features. *Chem. Soc. Rev.* **2010**, *39*, 4370–4387.
- (12) Gao, Z.; Moggi, L. V.; Miller, E. C.; Railsback, J. G.; Barnett, S. A. A perspective on low-temperature solid oxide fuel cells. *Energy Environ. Sci.* **2016**, *9*, 1602–1644.
- (13) Lacorre, P.; Goutenoire, F.; Bohnke, O.; Retoux, R.; Laligant, Y. Designing fast oxide-ion conductors based on La<sub>2</sub>Mo<sub>2</sub>O<sub>9</sub>. *Nature* **2000**, *404*, 856–858.
- (14) Wachsman, E. D.; Lee, K. T. Lowering the Temperature of Solid Oxide Fuel Cells. *Science* **2011**, *334*, 935–939.
- (15) Kubicek, M.; Cai, Z.; Ma, W.; Yildiz, B.; Hutter, H.; Fleig, J. Tensile Lattice Strain Accelerates Oxygen Surface Exchange and Diffusion in La<sub>1-x</sub>Sr<sub>x</sub>CoO<sub>3-δ</sub> Thin Films. *ACS Nano* **2013**, *7*, 3276–3286.
- (16) Shi, Y.; Bork, A. H.; Schweiger, S.; Rupp, J. L. The effect of mechanical twisting on oxygen ionic transport in solid-state energy conversion membranes. *Nat. Mater.* **2015**, *14*, 721–727.
- (17) Ishihara, T.; Matsuda, H.; Takita, Y. Doped LaGaO<sub>3</sub> perovskite type oxide as a new oxide ionic conductor. *J. Am. Chem. Soc.* **1994**, *116*, 3801–3803.
- (18) Sata, N.; Eberman, K.; Eberl, K.; Maier, J. Mesoscopic fast ion conduction in nanometre-scale planar heterostructures. *Nature* **2000**, *408*, 946–948.
- (19) Garcia-Barriocanal, J.; Rivera-Calzada, A.; Varela, M.; Sefrioui, Z.; Iborra, E.; Leon, C.; Pennycook, S. J.; Santamaria, J. Colossal Ionic Conductivity at Interfaces of Epitaxial ZrO<sub>2</sub>/Y<sub>2</sub>O<sub>3</sub>/SrTiO<sub>3</sub> Heterostructures. *Science* **2008**, *321*, 676–680.
- (20) Guo, X.; Maier, J. Ionically Conducting Two-Dimensional Heterostructures. *Adv. Mater.* **2009**, *21*, 2619–2631.
- (21) Su, Q.; Yoon, D.; Chen, A.; Khatkhatay, F.; Manthiram, A.; Wang, H. Vertically aligned nanocomposite electrolytes with superior out-of-plane ionic conductivity for solid oxide fuel cells. *J. Power Sources* **2013**, *242*, 455–463.
- (22) Lee, S.; Zhang, W.; Khatkhatay, F.; Jia, Q.; Wang, H.; MacManus-Driscoll, J. L. Strain Tuning and Strong Enhancement of Ionic Conductivity in SrZrO<sub>3</sub>-RE<sub>2</sub>O<sub>3</sub> (RE = Sm, Eu, Gd, Dy, and Er) Nanocomposite Films. *Adv. Funct. Mater.* **2015**, *25*, 4328–4333.
- (23) Zhang, L. X.; Chen, J.; Fan, L. L.; Dieguez, O.; Cao, J. L.; Pan, Z.; Wang, Y. L.; Wang, J. G.; Kim, M.; Deng, S. Q.; Wang, J. O.; Wang, H. H.; Deng, J. X.; Yu, R. B.; Scott, J. F.; Xing, X. R. Giant polarization in super-tetragonal thin films through interphase strain. *Science* **2018**, *361*, 494–497.
- (24) Gao, R.; Jain, A. C. P.; Pandya, S.; Dong, Y.; Yuan, Y.; Zhou, H.; Dedon, L. R.; Thoreton, V.; Saremi, S.; Xu, R.; Luo, A.; Chen, T.; Gopalan, V.; Ertekin, E.; Kilner, J.; Ishihara, T.; Perry, N. H.; Trinkle, D. R.; Martin, L. W. Designing Optimal Perovskite Structure for High Ionic Conduction. *Adv. Mater.* **2020**, *32*, No. 1905178.
- (25) Yang, S. M.; Lee, S.; Jian, J.; Zhang, W.; Lu, P.; Jia, Q.; Wang, H.; Won Noh, T.; Kalinin, S. V.; MacManus-Driscoll, J. L. Strongly enhanced oxygen ion transport through samarium-doped CeO<sub>2</sub> nanopillars in nanocomposite films. *Nat. Commun.* **2015**, *6*, No. 8588.
- (26) Lovett, A. J.; Wells, M. P.; He, Z.; Lu, J.; Wang, H.; MacManus-Driscoll, J. L. High ionic conductivity in fluorite δ-bismuth oxide-based vertically aligned nanocomposite thin films. *J. Mater. Chem. A* **2022**, *10*, 3478–3484.
- (27) Li, T.; Qing, D.; Liu, H.; Sun, S.; Li, H.; Hu, S.; Liu, S.; Xing, X.; Chen, J. Strong Room-Temperature Ferroelectricity in Strained SrTiO<sub>3</sub> Homoepitaxial Film. *Adv. Mater.* **2021**, *33*, No. 2008316.
- (28) Wang, Y.; Zhang, L.; Wang, J.; Li, Q.; Wang, H.; Gu, L.; Chen, J.; Deng, J.; Lin, K.; Huang, L.; Xing, X. Chemical-Pressure-Modulated BaTiO<sub>3</sub> Thin Films with Large Spontaneous Polarization and High Curie Temperature. *J. Am. Chem. Soc.* **2021**, *143*, 6491–6497.
- (29) Kendall, K. R.; Navas, C.; Thomas, J. K.; Loye, H.-C. z. Recent developments in perovskite-based oxide ion conductors. *Solid State Ionics* **1995**, *82*, 215–223.
- (30) Li, M.; Pietrowski, M. J.; De Souza, R. A.; Zhang, H.; Reaney, I. M.; Cook, S. N.; Kilner, J. A.; Sinclair, D. C. A family of oxide ion conductors based on the ferroelectric perovskite Na<sub>0.5</sub>Bi<sub>0.5</sub>TiO<sub>3</sub>. *Nat. Mater.* **2014**, *13*, 31–35.
- (31) Baiutti, F.; Chiabrera, F.; Acosta, M.; Diercks, D.; Parfitt, D.; Santiso, J.; Wang, X.; Cavallaro, A.; Morata, A.; Wang, H.; Chronos, A.; MacManus-Driscoll, J.; Tarancon, A. A high-entropy manganite in an ordered nanocomposite for long-term application in solid oxide cells. *Nat. Commun.* **2021**, *12*, No. 2660.
- (32) Labrincha, J. A.; Marques, F. M. B.; Frade, J. R. Protonic and oxygen-ion conduction in SrZrO<sub>3</sub>-based materials. *J. Mater. Sci.* **1995**, *30*, 2785–2792.
- (33) Kennedy, B. J.; Howard, C. J.; Chakoumakos, B. C. High-temperature phase transitions in SrZrO<sub>3</sub>. *Phys. Rev. B* **1999**, *59*, 4023.
- (34) Tian, H.; Mao, A. J.; Zhao, H. J.; Cui, Y.; Li, H.; Kuang, X. Y. Large polarization and dielectric response in epitaxial SrZrO<sub>3</sub> films. *Phys. Chem. Chem. Phys.* **2016**, *18*, 7680–7687.

(35) Shi, F.; Liang, K.; Qi, Z.-M. Investigation of the crystal structure, lattice vibration and dielectric property of SrZrO<sub>3</sub> ceramic. *J. Mater. Res.* **2016**, *31*, 3249–3254.

(36) Zhao, R.; Yang, C.; Wang, H.; Jiang, K.; Wu, H.; Shen, S.; Wang, L.; Sun, Y.; Jin, K.; Gao, J.; Chen, Li.; Wang, H.; MacManus-Driscoll, J.; van Aken, P.; Hong, J.; Li, W.; Yang, H. Emergent multiferroism with magnetodielectric coupling in EuTiO<sub>3</sub> created by a negative pressure control of strong spin-phonon coupling. *Nat. Commun.* **2022**, *13*, No. 2364.

(37) Linford, R. G.; Hackwood, S. Physical Techniques for the Study of Solid Electrolytes. *Chem. Rev.* **1981**, *81*, 327–364.

(38) Dyre, J. C.; Schröder, T. B. Universality of ac conduction in disordered solids. *Rev. Mod. Phys.* **2000**, *72*, 873–892.

(39) Yuan, X. Z.; Wang, H. J.; Sun, J. C.; Zhang, J. J. AC impedance technique in PEM fuel cell diagnosis—A review. *Int. J. Hydrogen Energy* **2007**, *32*, 4365–4380.

(40) Chang, B. Y.; Park, S. Electrochemical Impedance Spectroscopy. *Annu. Rev. Anal. Chem.* **2010**, *3*, 207–229.

(41) Lasia, A. Electrochemical Impedance Spectroscopy and its Applications. In *Modern Aspects of Electrochemistry*; Conway, B.; White, R., Eds.; Springer: New York, 2002; Vol. 35, pp 1–49.

(42) Wang, S. S.; Zhang, J. B.; Gharbi, O.; Vivier, V.; Gao, M.; Orazem, M. E. Electrochemical impedance spectroscopy. *Nat. Rev. Methods Primers* **2021**, *1*, 41.

(43) Lee, S.; Zhang, W.; Khatkhatay, F.; Wang, H.; Jia, Q.; MacManus-Driscoll, J. L. Ionic Conductivity Increased by Two Orders of Magnitude in Micrometer-Thick Vertical Yttria-Stabilized ZrO<sub>2</sub> Nanocomposite Films. *Nano Lett.* **2015**, *15*, 7362–7369.

(44) Fop, S.; McCombie, K. S.; Wildman, E. J.; Skakle, J. M. S.; Irvine, J. T. S.; Connor, P. A.; Savaniu, C.; Ritter, C.; McLaughlin, A. C. High oxide ion and proton conductivity in a disordered hexagonal perovskite. *Nat. Mater.* **2020**, *19*, 752–757.

(45) Zajac, W.; Rusinek, D.; Zheng, K.; Molenda, J. Applicability of Gd-doped BaZrO<sub>3</sub>, SrZrO<sub>3</sub>, BaCeO<sub>3</sub> and SrCeO<sub>3</sub> proton conducting perovskites as electrolytes for solid oxide fuel cells. *Open Chem.* **2013**, *11*, 471–484.

(46) Pennycook, S. J.; Jesson, D. E. High-resolution Z-contrast imaging of crystals. *Ultramicroscopy* **1991**, *37*, 14–38.

(47) Noh, H.-J.; Kim, B. J.; Oh, S. J.; Park, J. H.; Lin, H. J.; Chen, C. T.; Lee, Y. S.; Yamaura, K.; Takayama-Muromachi, E. Comparative study of the electronic structures of SrMO<sub>3</sub> (M = Ti, V, Mn, Fe, and Co; M = Zr, Mo, Ru, and Rh) by O 1s x-ray absorption spectroscopy. *J. Phys.: Condens. Matter* **2008**, *20*, No. 485208.

(48) Frati, F.; Hunault, M.; de Groot, F. M. F. Oxygen K-edge X-ray Absorption Spectra. *Chem. Rev.* **2020**, *120*, 4056–4110.

(49) Liang, X.; Shi, L.; Cao, R.; Wan, G.; Yan, W.; Chen, H.; Liu, Y.; Zou, X. Perovskite-Type Solid Solution Nano-Electrocatalysts Enable Simultaneously Enhanced Activity and Stability for Oxygen Evolution. *Adv. Mater.* **2020**, *32*, No. 2001430.

## Recommended by ACS

### Self-Powered Phase Transition Driven by Triboelectric Nanogenerator

Lele Ren, Junyi Zhai, *et al.*

MAY 09, 2023  
ACS APPLIED ELECTRONIC MATERIALS

READ 

### Operando Exploring and Modulating Phase Evolution Chemistry from MAX to MXenes in Molten Salt Synthesis

Shiqiang Wei, Li Song, *et al.*

MAY 02, 2023  
JOURNAL OF THE AMERICAN CHEMICAL SOCIETY

READ 

### Freestanding Oxide Membranes for Epitaxial Ferroelectric Heterojunctions

Muhammad Sheeraz, Tae Heon Kim, *et al.*

JULY 05, 2023  
ACS NANO

READ 

### Molecular Design of a Metal-Nitrosyl Ferroelectric with Reversible Photoisomerization

Wei-Jian Xu, João Rocha, *et al.*

JUNE 17, 2023  
JOURNAL OF THE AMERICAN CHEMICAL SOCIETY

READ 

Get More Suggestions >